Available online at www.sciencedirect.com
ScienceDirect
Journal of Computational Physics 227 (2008) 1722–1738
JOURNAL OF COMPUTATIONAL PHYSICS
www.elsevier.com/locate/jcp

Shape determination for deformed electromagnetic cavities

Volkan Akçelik *, Kwok Ko, Lie-Quan Lee, Zenghai Li, Cho-Kuen Ng, Liling Xiao

Advanced Computations Department, Stanford Linear Accelerator Center, Menlo Park, CA 94025, USA

Received 9 February 2007; received in revised form 10 August 2007; accepted 26 September 2007
Available online 13 October 2007

Abstract

The measured physical parameters of a superconducting cavity differ from those of the designed ideal cavity. This is due to shape deviations caused by both loose machine tolerances during fabrication and by the tuning process for the accelerating mode. We present a shape determination algorithm to solve for the unknown deviations from the ideal cavity using experimentally measured cavity data. The objective is to match the results of the deformed cavity model to experimental data through least-squares minimization. The inversion variables are unknown shape deformation parameters that describe perturbations of the ideal cavity. The constraint is the Maxwell eigenvalue problem. We solve the nonlinear optimization problem using a line-search based reduced space Gauss–Newton method where we compute shape sensitivities with a discrete adjoint approach. We present two shape determination examples, one from synthetic and the other from experimental data. The results demonstrate that the proposed algorithm is very effective in determining the deformed cavity shape.

Keywords: Shape optimization; Inverse problems; Eigenvalue problems; Maxwell equation; Linear accelerators

1. Introduction

The International Linear Collider (ILC) is a proposed electron–positron collider with global design efforts of hundreds of accelerator scientists and particle physicists from North America, Europe and Asia [25]. The ILC will answer such compelling questions as the identity of dark matter and the existence of extra dimensions. The heart of the ILC is the superconducting Radio Frequency (RF) electron and positron linacs (linear particle accelerators) which contribute to about 30% of the total cost. Each linac consists of 20,000 superconducting RF cavities. Due to high cost, the production tolerances in fabricating the cavity are loose. Thus, the cavity needs to be tuned at different locations to obtain the correct frequency and field flatness of the accelerating mode. This procedure changes the shape of the cavity from the designed one. The deformation of the cavity shape leads to changes in higher-order mode (HOM) frequencies, field distributions, and their damping

* Corresponding author. Tel.: +1 650 926 3574.
E-mail address: volkan@slac.stanford.edu (V. Akçelik).

0021-9991/$ - see front matter
doi:10.1016/j.jcp.2007.09.029

effects, which may result in beam instabilities. Therefore, it is important to determine the true dimensions of the real cavities for the reliable prediction of the HOM damping.

We formulate the shape determination problem as a PDE-constrained optimization problem. The constraint is the Maxwell eigenvalue problem. The objective is the weighted summation of the least-squares differences of the numerically computed and experimentally measured cavity data. The inversion variables are a set of parameters defining a perturbation from the designed cavity. The shape determination problem is akin to the inverse eigenvalue problem (IEP) [6,9,21]. IEP reconstructs a real symmetric matrix $\mathbf{A}(\mathbf{c}) \in \mathcal{R}^{n\times n}$ from prescribed spectral data, which consists of the complete or partial information of eigenvalues or eigenvectors. The unknown vector is $\mathbf{c} \in \mathcal{R}^n$, where the coefficient matrix $\mathbf{A}$ is an affine function of $\mathbf{c}$. The main difference is that, in the shape determination problem, the dependence of the objective functions and the mass and stiffness matrices on the unknown shape perturbation parameters is nonlinear and not known explicitly, while, in IEP, the coefficient matrix dependence on unknown parameters is linear and explicitly known.

To solve the resulting optimization problem we opt for a gradient-based method because of the large design space and considerable cost of solving the Maxwell eigenvalue problem for realistic three-dimensional cavities. The algorithm requires computations of derivatives of the objective function with respect to the unknown shape perturbation variables. We use an adjoint based method to compute the derivatives. In adjoint based methods, unlike direct sensitivity or finite difference methods, the total number of eigenvalue solves per gradient computation is independent of the number of shape perturbation variables [14].

Existing approaches to the adjoint based methods can be classified into two categories: *continuous* adjoint and *discrete* adjoint methods [2,5,14]. The continuous adjoint method follows a *differentiate-then-discretize* approach. One obtains optimality conditions in continuous forms and then discretizes the resulting expressions [2,10,17]. In the scope of shape optimization, one advantage of using continuous adjoint methods is the potential of converting continuous volume integrals to surface integrals, and thus helping to avoid volume mesh differentiation. However, the method still requires the differentiation of the surface representation. In addition, the surface integrals in gradient expressions require evaluations of higher-order derivatives of the state and adjoint field variables. Most importantly, the computed gradients are not always consistent with the true gradients in continuous adjoint methods [5,14].

The discrete adjoint method follows a *discretize-then-differentiate* approach. One first discretizes the governing equations and then differentiates the results [13,20]. The gradients computed from this method are always consistent with the discrete objective function. We use this method to compute derivatives when solving our shape determination problem. Unlike the continuous adjoint method, it requires mesh differentiation during gradient evaluations and computations of shape sensitivities of the stiffness and mass matrices. Since the unknown perturbation variables are small compared with the cavity dimensions in our problem, we move the mesh analytically according to the definition of each shape perturbation parameter so that the mesh movement is differentiable. Differentiability of the objective function with respect to design parameters requires mesh differentiability. This issue is discussed in the Appendix.

We use a line-search based reduced space Gauss–Newton (GN) algorithm to solve the nonlinear optimization algorithm. Since the inverse problem is typically ill-posed, we use regularization methods such as Tikhonov regularization and truncated singular value decomposition (T-SVD) [11]. Each nonlinear iteration requires the following operations:

1. Deform the mesh according to the current shape perturbation prediction,
2. Solve the forward problem, i.e. the Maxwell eigenvalue problem for each eigenmode involved in the least-squares minimization function,
3. Solve the adjoint problem,
4. Evaluate the Jacobian matrices,
5. Compute the reduced gradient and the reduced Gauss–Newton Hessian,
6. Compute the search direction for the new shape prediction.

The first four operations are performed in parallel due to the large problem size. The last two operations can be sequential since the design space is not large.

To examine the effectiveness of the algorithm, we present two numerical examples. The first one is a synthetic example. We first solve the Maxwell eigenvalue problem for a three-dimensional cavity deformed with a set of random shape perturbation parameters, and record the eigenfrequency and field information that will be used as synthetic data. To obtain the synthetic target data we use a relatively fine mesh. Then, we apply the above procedure to the inverse problem of determining the shape deformation using the synthetic data. For the inversion we use two different meshes model with different mesh sizes (both coarser than the target mesh), and perform numerical experiments with noisy and noise-free synthetic data, and with different regularization methods. This will provide a benchmark for the accuracy of the method. In the second example, we apply the method to compute the real shape of a cavity using the experimental mode frequencies and field values from the cavity data bank at DESY [8].

This article is organized as follows. Section 2 gives a basic outline of the shape determination algorithm, the formulation and the algorithm used to solve the nonlinear system. Section 3 presents the numerical examples. Section 4 then gives a brief summary.

2. Methods for shape determination problem

Our shape determination algorithm is based on a weighted least-squares minimization method. We formulate the problem as follows: let n denote the number of measured eigenvalues (λ), m denote the number of eigenmodes $\mathbf{E}$ for which the field measurements are available and p denote the number of electric field measurements for each eigenmode. The shape determination problem is the minimization of the following least-squares objective function $\mathcal{J}$, which is composed of two parts, the first $\mathcal{J}_\lambda$ being the eigenvalue misfit, and the second $\mathcal{J}_\mathrm{E}$ the electric field misfit:

$$\mathcal{J} = \mathcal{J}_\lambda + \mathcal{J}_\mathrm{E} = \frac{1}{2}\alpha \sum_{i=1}^{n} \left(\lambda_i - \bar{\lambda}_i\right)^2 + \frac{1}{2}\beta \sum_{i=1}^{m} \sum_{j=1}^{p} \left(\mathbf{E}_i(\mathbf{r}_j)\cdot \mathbf{n}_z - \overline{E}_j^i\right)^2, \tag{1}$$

where λ_i is the modeled eigenvalue of the ith mode, $\bar{\lambda}_i$ is the corresponding measured eigenvalue, α and β are weighting constants, $\mathbf{E}_i(\mathbf{r}_j) \in \mathbb{R}^3$ and $\overline{E}_j^i \in \mathbb{R}$ are modeled and measured electric field values of the ith eigenmode at location $\mathbf{r}_j$, and, $\mathbf{n}_z$ is the unit normal along the cavity axis. The choice of weighting constants α and β depends on relative values of eigenvalue and eigenmode sensitivities, and in addition to the accuracy of real-life measurements. (For instance the first 9 monopole mode measurements have relatively higher accuracy.)

Let $\mathbf{d} \in \mathbb{R}^{n_d}$ be the vector of n_d variables representing the unknown shape deviations of the ideal cavity. The electric field $\mathbf{E}_i$ and the eigenvalue λ_i present in (1) satisfy in the domain $\Omega(\mathbf{d})$, electric boundary $\Gamma_\mathrm{E}(\mathbf{d})$ and magnetic boundary $\Gamma_\mathrm{M}(\mathbf{d})$ (Fig. 1)

$$\nabla \times \left(\frac{1}{\epsilon}\nabla \times \mathbf{E}_i\right) - \lambda_i \mu \mathbf{E}_i = \mathbf{0} \quad \text{in } \Omega(\mathbf{d}), \tag{2}$$

$$\nabla \cdot \mathbf{E}_i = \mathbf{0} \quad \text{in } \Omega(\mathbf{d}), \tag{3}$$

$$\mathbf{n} \times \mathbf{E}_i = \mathbf{0} \quad \text{on } \Gamma_\mathrm{E}(\mathbf{d}), \tag{4}$$

$$\mathbf{n} \times \left(\frac{1}{\epsilon}\nabla \times \mathbf{E}_i\right) = \mathbf{0} \quad \text{on } \Gamma_\mathrm{M}(\mathbf{d}), \tag{5}$$

$$\frac{1}{2}\int_{\Omega_\mathbf{d}} \mu \mathbf{E}_i \cdot \mathbf{E}_i - \frac{1}{2} = 0, \tag{6}$$

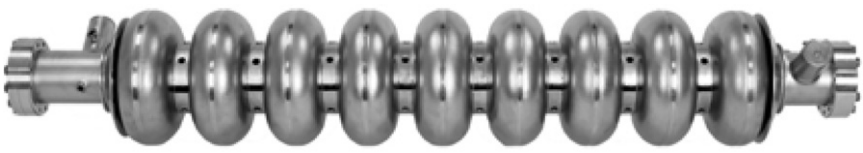

Fig. 1. 3D Geometry of 9 cell ILC coupler. All the outer boundaries are set to Γ_E.

where ϵ is the permittivity and μ the permeability. The ith eigenvalue is given by $\lambda_i = (\frac{2\pi f}{c})^2$, where c is the speed of light and f the eigenfrequency. For the remainder of the paper, we suppress the eigenvector and eigenvalue indices for ease of presentation unless where they are really needed.

There have been extensive studies on how to numerically solve the harmonic Maxwell's Eqs. (2)–(6). The use of Nedelec elements guarantees that solutions of the discretized problem from (2)–(6) with nonzero λ are divergence-free and physical [15,18]. We use the Nedelec finite element method, and discretize the electric field as $\mathbf{E} = \sum_{i=1}^{n_e} e_i \mathbf{N}_i$ where $\mathbf{N}_i$ are vector shape functions, e_i are the corresponding field intensities, and n_e is the number of degrees of freedom. The finite element discretization of the PDE-constrained optimization problem then yields

$$\begin{aligned} \underset{\mathbf{d}}{\text{minimize}} \quad & \mathcal{J} = \frac{1}{2}\alpha \Delta\lambda^{\mathrm{T}} \Delta\lambda + \frac{1}{2}\beta \sum_{i=1}^{m} (\Delta E^i)^{\mathrm{T}} \Delta E^i \\ \text{subject to} \quad & \mathbf{K}\mathbf{e} - \lambda \mathbf{M}\mathbf{e} = \mathbf{0}, \\ & \frac{1}{2}\mathbf{e}^{\mathrm{T}}\mathbf{M}\mathbf{e} = \frac{1}{2}, \end{aligned} \tag{7}$$

where $\mathbf{e} \in \mathbb{R}^{n_e}$ is the discrete electric field vector, the misfit vectors $\Delta\lambda \in \mathbb{R}^n$ and $\Delta E^i \in \mathbb{R}^p$ (i refers to the mode number) have elements

$$(\Delta\lambda)_j = \lambda_j - \bar{\lambda}_j, \tag{8}$$

$$(\Delta E^i)_j = \sum_{k=1}^{n_e} (\mathbf{e}_i)_k \mathbf{N}_k(\mathbf{r}_j) \cdot \mathbf{n}_z - \overline{E}^i_j, \tag{9}$$

and the stiffness matrix $\mathbf{K} \in \mathbb{R}^{n_e \times n_e}$ and mass matrix $\mathbf{M} \in \mathbb{R}^{n_e \times n_e}$ have elements

$$(\mathbf{K})_{ij} = \int_\Omega \frac{1}{\epsilon} \nabla \times \mathbf{N}_i \cdot \nabla \times \mathbf{N}_j \, \mathrm{d}\Omega, \tag{10}$$

$$(\mathbf{M})_{ij} = \int_\Omega \mu \mathbf{N}_i \cdot \mathbf{N}_j \, \mathrm{d}\Omega. \tag{11}$$

2.1. Optimality conditions

In order to derive the optimality conditions, we introduce the *adjoint variables* $\mathbf{t} \in \mathbb{R}^{n_e}$ and $\xi \in \mathbb{R}$. We then form a Lagrangian functional and enforce the constraint through the inner product of these variables. The adjoint vector $\mathbf{t}$ is also discretized with the Nedelec finite elements. The resulted Lagrangian functional $\mathcal{L}$ is:

$$\mathcal{L}(\mathbf{e}, \lambda, \mathbf{t}, \xi, \mathbf{d}) = \mathcal{J} + \mathbf{t}^{\mathrm{T}}(\mathbf{K}(\mathbf{d})\mathbf{e} - \lambda \mathbf{M}(\mathbf{d})\mathbf{e}) + \frac{1}{2}\xi(\mathbf{e}^{\mathrm{T}}\mathbf{M}(\mathbf{d})\mathbf{e} - 1). \tag{12}$$

The optimality conditions, or KKT conditions, require that at the optimum the Lagrangian has to be stationary with respect to its variables. We next derive the optimality conditions for (12).

2.1.1. State equation

The variation of Lagrangian functional with respect to the adjoint variables $\mathbf{t}$ and ξ gives the state equation for $\mathbf{e}$ and λ, which is the descretized form of the PDE-constraint (2)–(6).

$$\mathbf{K}\mathbf{e} - \lambda \mathbf{M}\mathbf{e} = \mathbf{0}, \tag{13}$$

$$\mathbf{e}^{\mathrm{T}}\mathbf{M}\mathbf{e} = 1. \tag{14}$$

In our simulations, we used a set of higher-order Nedelec type elements [15,18] to discretize (2)–(6). Note that matrix $\mathbf{K}$ and $\mathbf{M}$ are symmetric while $\mathbf{M}$ is also positive definite. In the large-scale accelerator cavity system simulations, these matrices can have sizes corresponding to hundreds of million degrees of freedom. A shift-and-invert Lanczos method has been implemented to solve (13) and (14) on parallel computers [16,23].

2.1.2. Adjoint equation

In order to obtain the adjoint equations we take the variation of (12) with respect to the state variables **e** and λ:

$$\mathbf{K}\mathbf{t} - \lambda\mathbf{M}\mathbf{t} + \xi\mathbf{M}\mathbf{e} = -\frac{\partial\mathcal{J}}{\partial\mathbf{e}}, \tag{15}$$

$$\mathbf{t}^{\mathrm{T}}\mathbf{M}\mathbf{e} = \frac{\partial\mathcal{J}}{\partial\lambda}. \tag{16}$$

There are as many adjoint equations, and adjoint pairs $(\mathbf{t},\xi)$ as the number of eigenpairs $(\mathbf{e},\lambda)$ involved in the objective function (1). Given state variables $(\mathbf{e},\lambda)$ and the inversion variable **d**, we compute the corresponding adjoint pair as follows. First we multiply Eq. (15) with $\mathbf{e}^{\mathrm{T}}$, yielding

$$\xi = -\mathbf{e}^{\mathrm{T}}\frac{\partial\mathcal{J}}{\partial\mathbf{e}}. \tag{17}$$

Next, given ξ, we solve for **t**

$$(\mathbf{K} - \lambda\mathbf{M})\mathbf{t} = -\xi\mathbf{M}\mathbf{e} - \frac{\partial\mathcal{J}}{\partial\mathbf{e}}. \tag{18}$$

Note that $\{\mathbf{e}\}$ is the null space of $\mathbf{K} - \lambda\mathbf{M}$. We use a sparse direct solver MUMPS [3,4] to calculate the solution of (18) and add a constant multiple of **e** to the solution such that the normalization condition (16) is satisfied.

2.1.3. Inversion equation

By taking the variation of Lagrangian with respect to inversion variable d_i we arrive at the expression for the ith component of the inversion equation:

$$\frac{\partial\mathcal{L}}{\partial d_i} = \frac{\partial\mathcal{J}}{\partial d_i} + \mathbf{t}^{\mathrm{T}}\left(\frac{\partial\mathbf{K}}{\partial d_i}\mathbf{e} - \lambda\frac{\partial\mathbf{M}}{\partial d_i}\mathbf{e}\right) + \frac{1}{2}\xi\mathbf{e}^{\mathrm{T}}\frac{\partial\mathbf{M}}{\partial d_i}\mathbf{e}, \tag{19}$$

where $\frac{\partial\mathbf{K}}{\partial d_i}$ and $\frac{\partial\mathbf{M}}{\partial d_i}$ are stiffness and mass matrix sensitivities. Since the amount of perturbations are very small with respect to the size of the cavity, we use analytical expressions for the mesh movement (see the Appendix). As a result, the mesh movement is continuous with respect to each design variable. In the case of large shape deformations, different alternatives are possible [12].

2.2. Optimization algorithm

To find the optimum shape, we need to solve three nonlinear equations (state, adjoint and inversion equations) for three sets of unknowns $(\mathbf{e},\lambda)$, $(\mathbf{t},\xi)$ and **d**. One approach is to solve nonlinear equations simultaneously. This is referred as the full space method [1]. An alternative is the reduced space method, where the state and adjoint unknowns are eliminated by solving the state and adjoint equations and the remaining nonlinear inversion equation is solved iteratively for the design variable. This work uses a reduced space method due to relatively small design space.

The reduced gradient can be computed as follows: given a set of shape perturbation estimate $\mathbf{d}_k$ at iteration k, we first solve the state equations (13) and (14) for the modes involved in the objective function (1). Then, using computed state variables (**e**, λ), we solve the adjoint equations (15) and (16) for the adjoint pairs $(\mathbf{t},\xi)$. Finally, using the state and adjoint variables, we compute the reduced gradient via (19).

Once the reduced gradient is computed, the inversion equation can be solved iteratively using the steepest descent or quasi-Newton methods. These methods only require gradient information. A better approach is to use the Gauss–Newton method which utilizes the least-squares structure of the problem. The Gauss–Newton method requires the so-called Jacobian matrices [19]. We define $\widetilde{\mathcal{J}}(\mathbf{d}) = \mathcal{J}(\mathbf{E}(\mathbf{d}),\lambda(\mathbf{d}),\mathbf{d})$, where the dependence of **E** and λ on **d** is implicit through the state equation. Then, the reduced gradient can be written in terms of the Jacobian matrices

$$\mathbf{g}_d := \nabla_d\widetilde{\mathcal{J}}(\mathbf{d}) = \nabla_d\widetilde{\mathcal{J}}_\lambda + \nabla_d\widetilde{\mathcal{J}}_{\mathrm{E}} = \alpha\mathbf{J}_\lambda^{\mathrm{T}}\Delta\lambda + \beta\sum_{j=1}^{m}(\mathbf{J}_{\mathrm{E}}^j)^{\mathrm{T}}\Delta E^j, \tag{20}$$

where Jacobians $\mathbf{J}_\lambda \in \mathbb{R}^{n\times n_d}$ and $\mathbf{J}_\mathrm{E} \in \mathbb{R}^{p\times n_d}$ are defined as:

$$(\mathbf{J}_\lambda)_{ij} = \frac{\partial \lambda_i(\mathbf{d})}{\partial d_j}, \tag{21}$$

$$(\mathbf{J}^p_\mathrm{E})_{ij} = \frac{\partial \Delta E^p_i(\mathbf{d})}{\partial d_j}. \tag{22}$$

For the shape determination problem, the size of the inversion space is relatively small. For an ILC cavity shape, a typical number of inversion parameters is less than one hundred, (unlike state and adjoint variables, which are in the order of millions). Consequently, it is feasible to compute and store the Jacobians.

The reduced Gauss–Newton (GN) Hessian $\mathbf{W}_\mathrm{GN} \in \mathbb{R}^{n_d\times n_d}$ is:

$$\mathbf{W}_\mathrm{GN} := \alpha \mathbf{J}_\lambda^\mathrm{T}\mathbf{J}_\lambda + \beta \sum_{j=1}^{m} (\mathbf{J}^j_\mathrm{E})^\mathrm{T}\mathbf{J}^j_\mathrm{E}. \tag{23}$$

As misfits $\Delta\lambda$ and ΔE^j approach zero, the GN Hessian approaches to the true Hessian.

In order to solve the nonlinear equation we employ the Gauss–Newton method with an Armijo-based line search strategy. Because of the positive-definiteness of the GN Hessian, this method is known to be globally convergent. Furthermore, the number of nonlinear iterations for the Gauss–Newton method to converge is small and independent of the number of design parameters [19].

2.2.1. Computing the Jacobians

The elements of $\mathbf{J}_\lambda$ and $\mathbf{J}_\mathrm{E}$ can be computed using (19). In (19) the function $\mathcal{J}$ is equivalent to λ_i for $\mathbf{J}_\lambda$, and to ΔE^j for $\mathbf{J}^j_\mathrm{E}$ terms. The state variables $\mathbf{e}$ and λ are the corresponding electric field, and eigenvalues of the related mode. The adjoint variables are computed via Eqs. (15 and 16) with the corresponding source terms.

For $\mathbf{J}_\lambda$, each term can be computed as:

$$(\mathbf{J}_\lambda)_{ij} = \mathbf{t}_i^\mathrm{T}\left(\frac{\partial \mathbf{K}}{\partial d_j}\mathbf{e}_i - \lambda_i \frac{\partial \mathbf{M}}{\partial d_j}\mathbf{e}_i\right) + \frac{1}{2}\xi_i \mathbf{e}_i^\mathrm{T}\frac{\partial \mathbf{M}}{\partial d_j}\mathbf{e}_i, \tag{24}$$

where adjoint pairs $(\mathbf{t}, \xi)$ are the solution of

$$\begin{bmatrix} \mathbf{K}-\lambda\mathbf{M} & \mathbf{Me} \\ (\mathbf{Me})^\mathrm{T} & \mathbf{0} \end{bmatrix}\begin{pmatrix} \mathbf{t} \\ \xi \end{pmatrix} = \begin{pmatrix} 0 \\ 1 \end{pmatrix}. \tag{25}$$

For eigenvalue sensitivity calculations, an inspection of Eq. (25) reveals that the adjoint vector $\mathbf{t}$ is simply eigenvector $\mathbf{e}$, and adjoint value $\xi = 0$. Hence, $\mathbf{J}_\lambda$ requires no extra computation for adjoint variables, and demands the evaluation of (24) only for each $\mathbf{J}_\lambda$ term.

Similarly for a term of $\mathbf{J}^l_\mathrm{E}$, the expression is:

$$(\mathbf{J}^l_\mathrm{E})_{ij} = \sum_{r=1}^{n_e} (\mathbf{e}_l)_r \frac{\partial \mathbf{N}_r(\mathbf{r}_i)}{\partial d_j}\cdot \mathbf{n}_z + \mathbf{t}_i^\mathrm{T}\left(\frac{\partial \mathbf{K}}{\partial d_j}\mathbf{e}_l - \lambda_l \frac{\partial \mathbf{M}}{\partial d_j}\mathbf{e}_l\right) + \frac{1}{2}\xi_i \mathbf{e}_l^\mathrm{T}\frac{\partial \mathbf{M}}{\partial d_j}\mathbf{e}_l, \tag{26}$$

where the adjoint eigenpairs $\mathbf{t}$, ξ are solution of

$$\begin{bmatrix} \mathbf{K}-\lambda\mathbf{M} & \mathbf{Me} \\ (\mathbf{Me})^\mathrm{T} & 0 \end{bmatrix}\begin{pmatrix} \mathbf{t} \\ \xi \end{pmatrix} = \begin{pmatrix} \mathbf{h} \\ 0 \end{pmatrix}, \tag{27}$$

where the source term $h_j = -\sum_{k=1}^{n_e}\delta_{jk}\mathbf{N}_k(\mathbf{r}_i)\cdot\mathbf{n}_z$. To compute $\mathbf{J}_\mathrm{E}$, we solve Eq. (27) for $p\times m$ times, and evaluate (26) for each $\mathbf{J}_\mathrm{E}$ term.

2.3. Regularization methods

The unknown deformed cavity shape has an infinite number of degrees of freedom. On the other hand, the measured cavity information is finite, and only a limited number of eigenfrequencies and field values are available. Due to this lack of information, the shape determination problem is typically ill-posed. To remedy

ill-posedness and rank deficiency the PDE-constrained problem has to be regularized. The choice of regularization technique and regularization parameters are crucial in the success of the inversion algorithm. The selection depends on several factors such as the uncertainties in the measurements and in the inversion parameters, and amount of available spectral data [24]. Two different regularization methods, *Tikhonov regularization* and *Truncated singular value decomposition* (*T-SVD*) are used in this work.

2.3.1. Tikhonov regularization

In Tikhonov regularization one adds an extra function to the objective function. The standard Tikhonov regularization function has the following form:

$$R(\mathbf{d}) = \sum_{i=1}^{n_d} \gamma_i d_i^2,$$

where γ_i are the regularization constant and in general can attain different values for each inversion parameter.

2.3.2. T-SVD regularization

One method of overcoming rank deficiency and ill-posedness is to use truncated singular value decomposition (T-SVD) with the GN method [11].

The singular value decomposition (SVD) of the reduced Hessian is equivalent to eigenvalue decomposition and is of the form

$$\mathbf{W}_{\mathrm{GN}} = \sum_{i=1}^{n_d} \frac{1}{2}\sigma_i \mathbf{v}_i^{\mathrm{T}}\mathbf{v}_i, \tag{28}$$

where σ_i are singular values and $\mathbf{v}_i$ singular vectors. In the case where the $\mathbf{W}_{\mathrm{GN}}$ is ill-posed and rank-deficient, T-SVD just simply ignores the SVD components associated with singular values less than some threshold value. The search direction of the GN method then becomes

$$\mathbf{p}_k = -\sum_{j=1} \frac{\mathbf{v}_j^{\mathrm{T}}\mathbf{g}_d}{\sigma_j}\mathbf{v}_j, \tag{29}$$

where j includes the set of singular values satisfying $\sigma_j > \kappa$. The choice of κ plays the role of the regularization parameter.

2.3.3. Outline of the algorithm

We have described the components of the nonlinear algorithm. The outline of the shape determination algorithm is then

- Select the set of inversion variables for the deformed cavity [27]. Choose the ideal cavity as the initial guess (this is equivalent to setting $\mathbf{d} = \mathbf{0}$).
- Create a CAD model of the ideal cavity, and create a tetrahedral mesh using the mesh generation tool CUBIT [7].
- While not converged at iteration k:
  1. Solve the Maxwell eigenvalue problem for the modes involved in the objective function for state variables $(\mathbf{e}, \lambda)$.
  2. Solve the adjoint problems for the adjoint pairs $(\mathbf{t}, \xi)$.
  3. Compute the Jacobian matrices.
  4. Compute the reduced gradient and reduced GN Hessian.
  5. Compute the search direction $\mathbf{p}_k \in \mathbb{R}^{n_d}$ by solving $\mathbf{W}_{\mathrm{GN}}\mathbf{p}_k = -\mathbf{g}_d$.
  6. Update the current shape iterate with $\mathbf{d}_{k+1} = \mathbf{d}_k + \alpha\mathbf{p}_k$. Move the mesh for the new design variable $\mathbf{d}_{k+1}$. Here, $\alpha \in \mathbb{R}$ is the step length determined by Armijo-based backtracking algorithm.

Convergence criteria will be discussed in the next section.

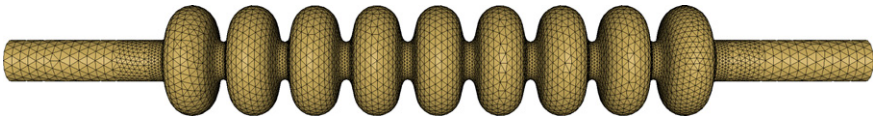

Fig. 2. 3D mesh of ILC TDR 9 cells cavity used in the synthetic example.

3. Numerical examples

In this section we present two numerical examples. Both examples use realistic 3D cavities. The first example uses synthetically obtained data, while the second one real cavity data as input to recover the deformed cavity shape.

3.1. Shape determination with synthetic data

The effectiveness of the prescribed method to predict deformed cavity shape is first assessed with a synthetic example. We choose a three-dimensional ILC TDR 9 cells cavity without couplers. First, we create a CAD model and several tetrahedral meshes for the ideal cavity with different mesh sizes. In this work, we use second order Nedelec finite element for the discretization (Fig. 2).

The next step is to deform the cavity using a random deformation set. We choose the following perturbations as independent shape parameters: for each cell the change in the ideal cell radius (dr), the change in the ideal cell length in longitudinal direction (dz), and four parameters representing cell tuning procedure (dt1, dt2, dt3, dt4), for each iris the change in the ideal iris thickness (da). In total, the deformation set has 62 independent perturbation parameters (for each of the 9 cells dr, dz, dt1, dt2, dt3 and dt4, and for each of 8 irises da). We assign a random value for each of these variables (Table 1), deform the ideal cavity along them, and move the mesh accordingly. We refer to this artificially deformed cavity as the *target cavity*. Next step is solving the Maxwell eigenvalue problem for the target cavity using a fine mesh[1] with 6 million degrees of freedom, and compute the first 45 modes with nonzero eigenvalues (the first 9 are the monopole modes, and the remaining 36 are the HOM modes). We also record 9 field values at the center of each cell per mode for the first 9 monopole modes. In other words, in Eq. (1) we use 45 modes for $\mathcal{J}_f$ and 9 modes with 9 field values for $\mathcal{J}_E$. The weighting constants α is set to 1, and β to 10.

We use the recorded data of the target cavity to recover the unknown shape perturbations. The ideal cavity shape is used as the initial guess. The inversion variable set is the same set used for the random deformation. We refer to the resulted shape as *inverted cavity*. The reduced GN Hessian of the synthetic problem with this set of parameters is ill-posed. The spectra of GN Hessian for different mesh discretization are shown in Fig. 3. It is evident from the spectra that any eigenvalue information of GN Hessian with values less than 1e6 is in the noise level. To remedy ill-posedness, we use either Tikhonov regularization with regularization constant $\gamma = 1e6$, or T-SVD method with cut-off frequency $\kappa = 1e6$. We solve the inverse problem using two different mesh discretizations, with 2.48e6 (*dense mesh*) and 0.85e6 (*coarse mesh*) degrees of freedom models. We perform five different inversion tests, using different mesh models, noise-free and noisy data, and different regularization techniques:

Case 1: Using dense mesh, with noise-free data, and Tikhonov regularization.
Case 2: Using dense mesh, with noisy data, and Tikhonov regularization.
Case 3: Using dense mesh, with noisy data, and T-SVD regularization.
Case 4: Using coarse mesh, with noisy data, and Tikhonov regularization.
Case 5: Using coarse mesh, with noisy data, and T-SVD regularization.

[1] Our numerical experiments indicate that eigenfrequencies obtained using this mesh is accurate to 1 KHz level, and normalized field values are accurate to the fourth digit.

Table 1
Inverted and target cavity shape dimensions

Parameter	Target	Case 1D + F + TR	Case 2D + N + TR	Case 3D + N + TS	Case 4C + N + TR	Case 5C + N + TS
Cell 1 dr	300	207	217	38	41	36
Cell 1 dz	−300	−237	−242	−145	−239	−113
Cell 1 dt1	100	−15	−15	74	−41	48
Cell 1 dt2	300	47	57	135	60	159
Cell 1 dt3	100	28	29	−2	55	65
Cell 1 dt4	−200	−174	−163	−244	−187	−321
Cell 2 dr	300	155	158	271	106	300
Cell 2 dz	−300	−301	−310	−345	−307	−404
Cell 2 dt1	100	142	149	250	136	271
Cell 2 dt2	300	59	46	98	48	114
Cell 2 dt3	100	60	71	218	113	343
Cell 2 dt4	−200	−109	−113	−222	−121	−205
Cell 3 dr	300	109	119	342	88	100
Cell 3 dz	−300	−294	−284	−305	−279	−267
Cell 3 dt1	100	102	95	115	84	24
Cell 3 dt2	300	70	75	77	77	57
Cell 3 dt3	100	70	56	84	87	12
Cell 3 dt4	−200	−122	−123	−221	−132	−136
Cell 4 dr	300	131	140	225	111	115
Cell 4 dz	−300	−290	−296	−243	−294	−246
Cell 4 dt1	100	92	92	110	82	87
Cell 4 dt2	300	78	71	131	70	33
Cell 4 dt3	100	72	79	63	110	112
Cell 4 dt4	−200	−137	−143	−230	−144	−246
Cell 5 dr	300	102	103	201	87	208
Cell 5 dz	−300	−285	−286	−291	−287	−316
Cell 5 dt1	100	86	79	120	70	177
Cell 5 dt2	300	87	85	129	80	181
Cell 5 dt3	100	85	80	114	101	261
Cell 5 dt4	−200	−142	−144	−204	−143	−231
Cell 6 dr	300	140	119	343	82	199
Cell 6 dz	−300	−277	−271	−318	−276	−293
Cell 6 dt1	100	81	85	106	78	22
Cell 6 dt2	300	98	106	65	99	65
Cell 6 dt3	100	77	76	108	108	47
Cell 6 dt4	−200	−158	−145	−235	−146	−153
Cell 7 dr	300	144	171	311	162	159
Cell 7 dz	−300	−272	−276	−254	−285	−266
Cell 7 dt1	100	75	73	115	65	70
Cell 7 dt2	300	112	98	131	86	4
Cell 7 dt3	100	84	81	130	114	139
Cell 7 dt4	−200	−168	−172	−301	−167	−268
Cell 8 dr	300	159	159	311	152	296
Cell 8 dz	−300	−264	−255	−271	−266	−248
Cell 8 dt1	100	66	71	151	63	211
Cell 8 dt2	300	147	154	304	140	367
Cell 8 dt3	100	98	89	151	116	281
Cell 8 dt4	−200	−185	−188	−231	−177	−281
Cell 9 dr	300	16	−12	114	54	139
Cell 9 dz	−300	−263	−261	−395	−276	−429
Cell 9 dt1	100	45	45	15	36	2
Cell 9 dt2	300	−39	−41	−91	−53	−136
Cell 9 dt3	100	−63	−56	−16	−75	−46
Cell 9 dt4	−200	−40	−41	3	−13	81

Table 1 (*continued*)

Parameter	Target	Case 1D + F + TR	Case 2D + N + TR	Case 3D + N + TS	Case 4C + N + TR	Case 5C + N + TS
Iris 1 da	100	112	120	111	100	65
Iris 2 da	100	118	113	90	94	86
Iris 3 da	100	121	124	121	104	124
Iris 4 da	100	124	116	120	95	86
Iris 5 da	100	127	129	125	106	115
Iris 6 da	100	130	135	119	113	126
Iris 7 da	100	131	132	106	110	80
Iris 8 da	100	132	128	110	106	74

All parameters are in μm. D: dense mesh, C: coarse mesh, F: noise-free data, N: noisy data, TR: Tikhonov regularization, TS: T-SVD regularization.

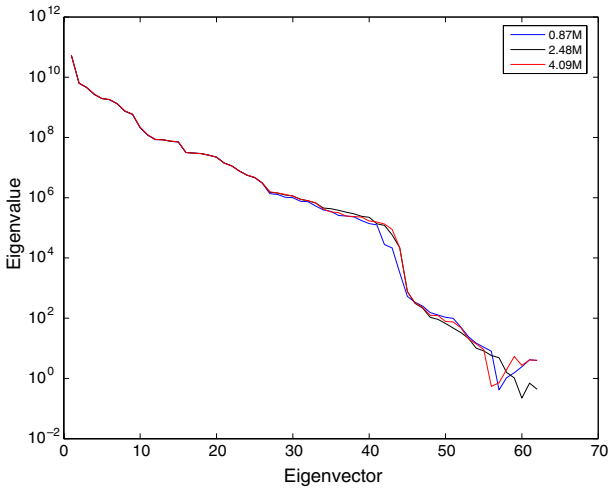

Fig. 3. Eigenvalue spectra of reduced Hessian obtained using meshes with different densities.

In this work, noise refers to the accuracy of the eigenvector and eigenvalue measurement. We assume that the synthetic frequencies are accurate to 1e3 Hz level for the monopole modes, and to 1e4 Hz level for the HOM modes. For the field data, the normalized electric field values are assumed to be accurate to the third digit. For example, a target HOM frequency of 1,623,189,138 Hz is converted to 1,623,190,000 Hz for the noisy data. The assumptions on the noise level are in agreement with the accuracy of the measurements [8].

The nonlinear algorithm terminates when one of the following criteria is achieved: (i) the relative norm of the reduced gradient is decreased by a factor of 1e5, or (ii) the norm of the reduced GN Newton search direction is less than 1 μm. In all five cases the nonlinear algorithm converges in 4 nonlinear iterations. Inverted and target cavity shape parameters are listed in Table 1. Fig. 4 shows the misfit in eigenfrequencies with the target data for the ideal and deformed cavity, and Fig. 5 shows the misfit in normalized electric field values for 9 monopole modes both for the ideal and deformed cavities.

From five different inversion cases, we have the following conclusions:

- The misfit both in eigenfrequencies and electric field values decreases to the noise level for all five cases. Noisy data doesn't influence the inversion results.
- The inverted shape parameters are in good agreement with the target parameters for dz and da values. The situation for the other parameters is more complicated. Results indicate that for the end cells dr, dt1, dt2, dt3 and dt4 are strongly correlated. Their correlation is relatively weaker for the inner cells.

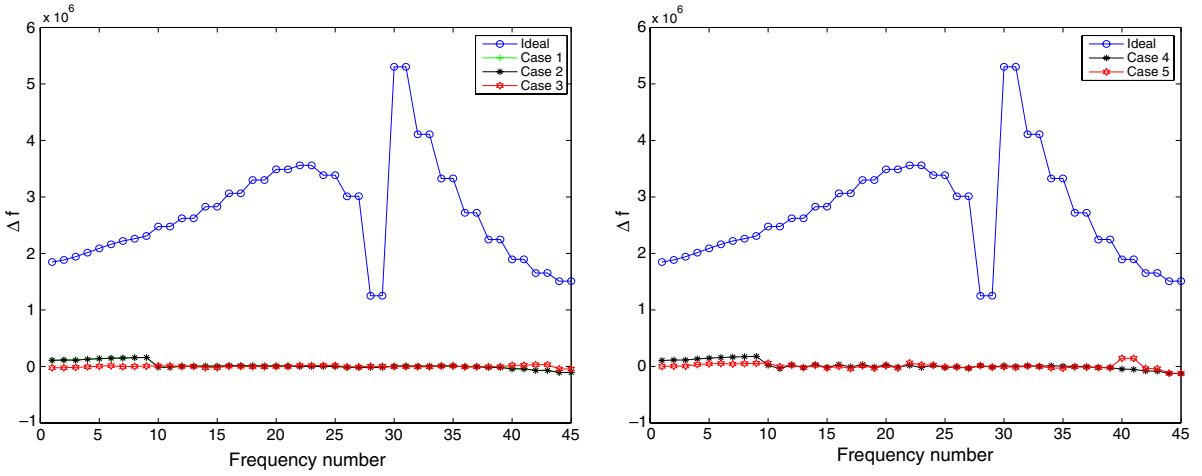

Fig. 4. Error in frequency values for the initial and inverted cavities for the first 45 frequencies. Left: using dense mesh, right: using coarse mesh.

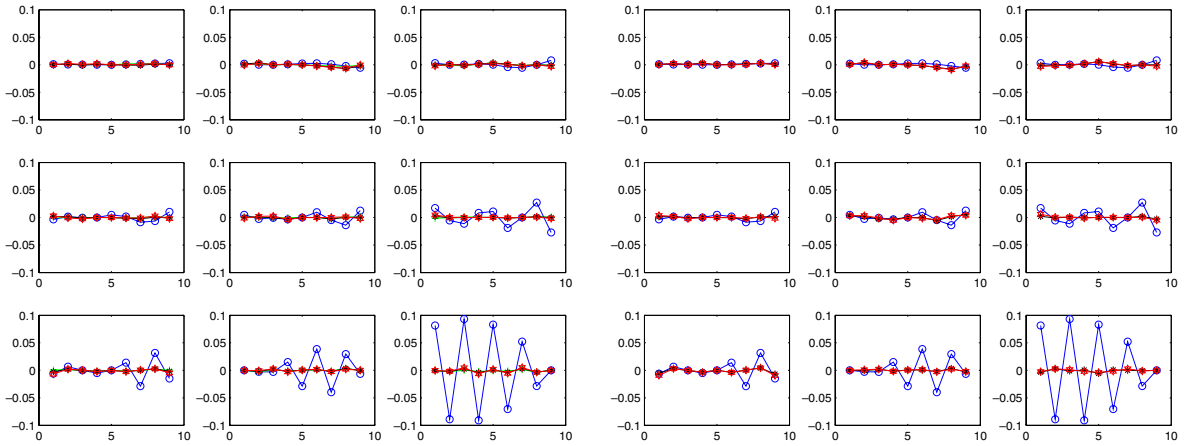

Fig. 5. Error in normalized field values for the initial and inverted cavities for the first 9 monopole modes. Left: using dense mesh, right: using coarse mesh. Case numbers are as in Fig. 4.

- We have ample numerical evidences that inversion results correspond to global minima (once regularization method is chosen the optimizer converges to a unique minimum starting from different initial guesses).
- The variation in the inversion results shows the importance of regularization methods.
- The dense mesh performs better than the coarse mesh. The results suggest that the discrete model should be accurate to the noise level.
- For the synthetic problem T-SVD regularization performs better in estimating inversion variables. The best inversion results are obtained in Case 3.

3.2. Shape determination with real data

DESY [8] provides experimental results for manufactured ILC baseline cavities. In particular, the DESY cavity database includes measurements of 9 monopole mode frequencies, HOM frequencies, and the field value measured at the center of each cell for the monopole modes. We use the available

experimental data for one of the manufactured and tuned 9 cells cavities to infer for the deviations of the ideal cavity shape.

The ideal cavity shape includes couplers at the end-groups, and is discretized with quadratic tetrahedral elements, resulting in 3.6 million degrees of freedom (Fig. 6). As expected, due to shape deviations, the mode frequencies of the ideal cavity do not agree with those of the real cavity. We use the shape determination algorithm presented in the previous section to determine the unknown cavity deviations with the following set as shape variables:

- For each cell, the change in the cell radius.
- For each cell, two parameters defining cell warping perpendicular to the cavity axis.
- For each cell, four parameters representing the tuning procedure.
- For each cell, the change in the cell thickness.
- For each iris, the change in the iris thickness.

In total, there are 80 unknown parameters defining the shape deviation. The selection of this set includes all the potential degrees of freedom that both has sensitivity the objective function, and known to have uncertainties in the manufacturing process. In general, we choose the set of unknown shape parameters such that the resulted inversion variable is a good approximation of the potential shape deformation [8,27]. We use the following measurement data in this example: The $\mathcal{J}_{\mathrm{f}}$ includes the 9 monopole frequencies and 36 HOM frequencies, and $\mathcal{J}_{\mathrm{E}}$ the field values for the 9 monopole modes. The weighting constant α is 10 for the monopole modes, and 1 for the HOM modes, and β is 10 for the field value misfit.

The optimization problem with the given design parameters and available data is ill-posed and rank deficient. Fig. 7 shows the eigenvalue spectrum of the GN Hessian. As regularization method we use T-SVD regularization and set the regularization parameter $\kappa = \frac{\sigma_{\max}}{10^5}$.

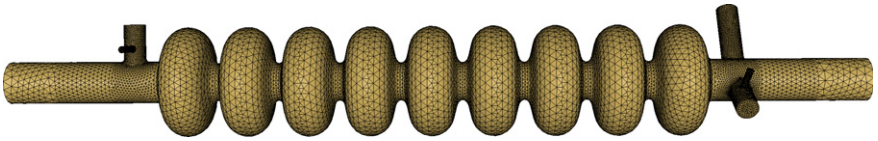

Fig. 6. ILC TDR 9 cells cavity with couplers.

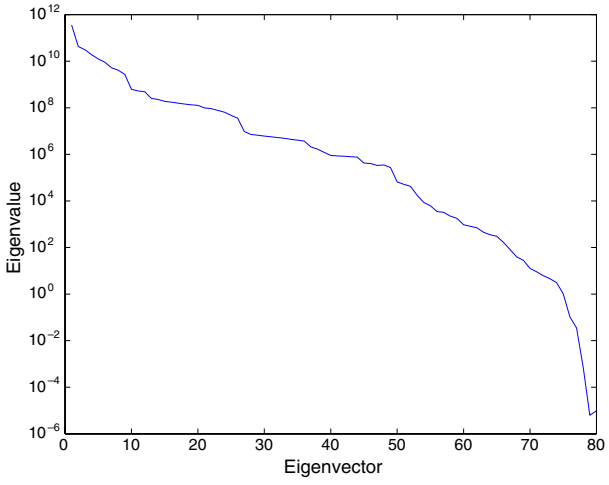

Fig. 7. Eigenvalue spectrum of the GN Hessian for real data inversion.

We use the ideal cavity as the initial guess, and assume convergence when the decrease in objective function is less than a certain tolerance. The algorithm converges in 7 nonlinear iterations (Fig. 8).

As expected, the resulted inverted cavity shape is only a small perturbation of the real cavity. The typical size of an inverted parameter is at the order of 100 μm. These are relatively small values compared to the size of the ideal cavity (the diameter of each cell is 10.33 cm, and the length of the cavity is about 1 m).

Fig. 9 shows the frequency differences with respect to the measured data, for both the ideal and the deformed cavities. Since the measurements of the monopole frequencies have higher fidelity, we use a larger weight α for the monopole frequency misfit. As a result, the inverted cavity data have better agreement with the real cavity for the monopole modes than for the HOM modes.

In addition to the frequency data, monopole mode fields for the first 9 modes are also used for the optimization. Fig. 10 shows the differences of the field values with respect to measured data. With respect to the monopole mode field distributions, the inverted cavity has very good agreement with the measured data.

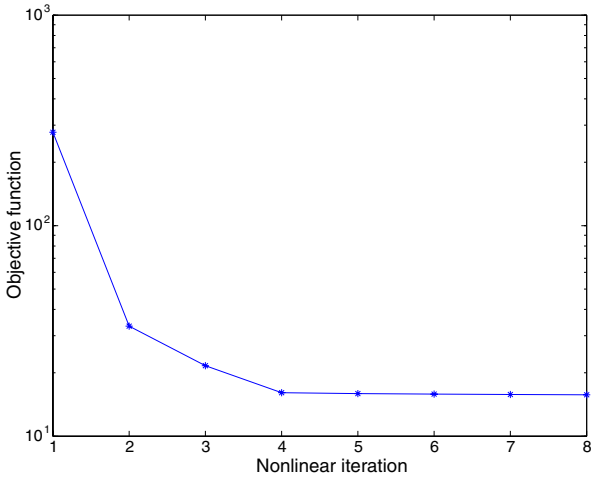

Fig. 8. Change in the objective function with nonlinear iterations.

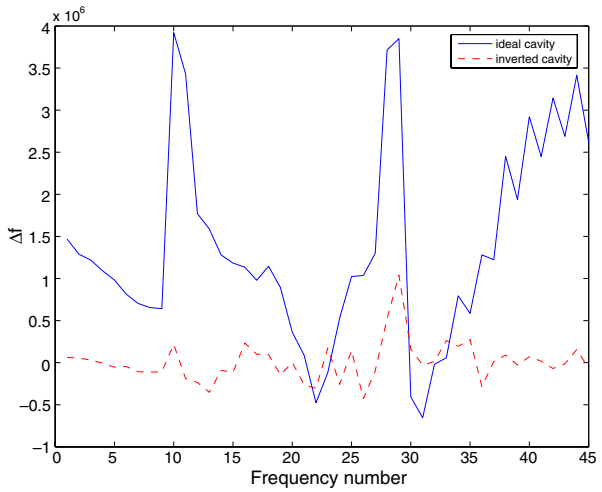

Fig. 9. Frequency differences for the ideal cavity and inverted deformed cavity.

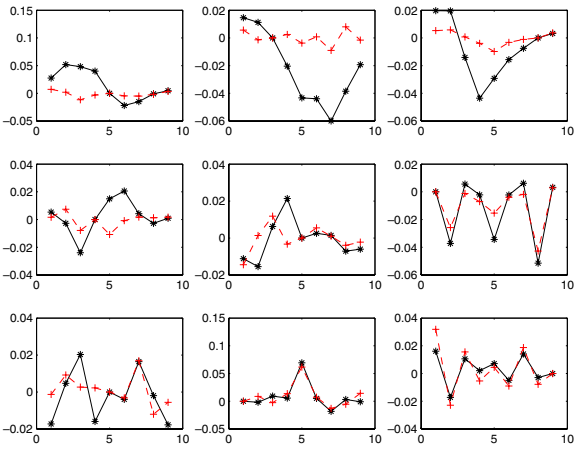

Fig. 10. Error in the normalized field values for the 9 monopole modes.

4. Summary

We have presented a Maxwell eigenvalue shape determination algorithm for solving unknown perturbations of cavities through least-squares minimization. We used a reduced space Gauss–Newton method, derived the nonlinear optimality system, and outlined the components of the optimization algorithm.

We presented two test examples to examine the effectiveness of the algorithm. The first is a synthetic example, where the deformed cavity shape and the inversion parameter set are known. We performed the inversion example using two different meshes, where the target data is obtained using a much finer mesh. Since this is a synthetic problem, it is possible to check the quality of the result. The synthetic example demonstrates that the algorithm successfully inverts for the deformed cavity. However, due to ill-posedness and rank deficiency, quality of the inversion results depends on several factors, the most important of which is the choice of the regularization method.

The second example uses real data and the exact solution is not known. As regularization method the GN method with T-SVD was used for solving the problem. The algorithm yields a deformed cavity with frequency and field values very close to those of the recorded real cavity.

Further studies on the effect of the null space of the inversion variable, error analysis of the input data and of the ill-posedness of the shape determination problem will be pursued in the future.

Acknowledgments

This work was partially supported by Stanford Linear Accelerator Center SLAC/DOE Contract DE-AC02-76-SF00515. Part of this research used resources of the National Center for Computational Sciences at Oak Ridge National Laboratory, which is supported by the Office of Science of the US Department of Energy under Contract No. DE-AC05-00OR22725. This research also used resources of the National Energy Research Scientific Computing Center, which is supported by the Office of Science of the US Department of Energy under Contract No. DE-AC03-76SF00098.

The authors thank the anonymous referees for many constructive comments that improved this paper.

Appendix

Here, we present formulations for the shape derivatives of the objective function. The Lagrangian of the discrete PDE constrained optimization problem is

$$\mathcal{L}(\mathbf{e},\mathbf{t},\lambda,\xi,\mathbf{d}) = \mathcal{J}(\mathbf{d}) + \mathbf{t}^{\mathrm{T}}(\mathbf{K}(\mathbf{d})\mathbf{e} - \lambda\mathbf{M}(\mathbf{d})\mathbf{e}) + \frac{1}{2}\xi\mathbf{e}^{\mathrm{T}}\mathbf{M}(\mathbf{d})\mathbf{e}. \tag{30}$$

The first order optimality conditions require that the variation of Lagrangian must be zero with respect to the state, adjoint and inversion variables. The variation of the Lagrangian with respect to the state and adjoint variables leads to the state (2)–(6) and adjoint Eqs. (15) and (16). The variation with respect to the inversion variable d_r yields the inversion equation

$$\frac{\partial \mathcal{L}}{\partial d_r} = \frac{\partial \mathcal{J}}{\partial d_r} + \mathbf{t}^{\mathrm{T}}\left(\frac{\partial \mathbf{K}}{\partial d_r}\mathbf{e} - \lambda \frac{\partial \mathbf{M}}{\partial d_r}\mathbf{e}\right) + \frac{1}{2}\xi \mathbf{e}^{\mathrm{T}}\frac{\partial \mathbf{M}}{\partial d_r}\mathbf{e}. \tag{31}$$

Differentiability of the reduced gradient requires differentiability of the objective function $\mathcal{J}$, and mass and stiffness matrices with respect to the shape parameters.

It is advantageous to work in curvilinear coordinate system. The transformation from the physical coordinate $\mathbf{x}$ to the curvilinear coordinate $\boldsymbol{\zeta}$ is given by

$$\mathbf{x} \equiv \mathbf{x}(\zeta_1, \zeta_2, \zeta_3). \tag{32}$$

The vector shape function $\mathbf{N}_i$ for a triangular element can be computed using curvilinear coordinates [22,26],

$$\mathbf{N}_i = \sum_{k=1}^{3} N_{ik}(\zeta_1, \zeta_2, \zeta_3)\nabla\zeta_k, \tag{33}$$

where $N_{ik}(\zeta_1, \zeta_2, \zeta_3)$ are polynomial functions [26]. The term $\nabla\zeta_k$ is defined as

$$\nabla\zeta_k = \begin{bmatrix} \frac{\partial \zeta_k}{\partial x} \\ \frac{\partial \zeta_k}{\partial y} \\ \frac{\partial \zeta_k}{\partial z} \end{bmatrix}. \tag{34}$$

The shape derivative of the objective function $\mathcal{J}$ (Eq. (1)) is given as

$$\frac{\partial \mathcal{J}}{\partial d_r} = \beta \sum_{i=1}^{m}\sum_{j=1}^{p}\left[(\Delta E^i)_j\left(\sum_{k=1}^{n_e}(\mathbf{e}_i)_k \frac{\partial \mathbf{N}_k(\mathbf{r}_j)}{\partial d_r}\cdot \mathbf{n}_z\right)\right], \tag{35}$$

where

$$\frac{\partial \mathbf{N}_k(\mathbf{r_i})}{\partial d_r} = \sum_{l=1}^{3} N_{kl}(\zeta_1, \zeta_2, \zeta_3)\frac{\partial \nabla\zeta_l(\mathbf{r}_i)}{\partial d_r}, \tag{36}$$

here the important term is the derivative of $\nabla\zeta_l$ with respect to the design variable d_r. Its computation will be explained below.

To compute the shape sensitivity of the stiffness matrix, first we define the curl of vector shape functions. Taking the curl of (33) yields

$$\nabla \times \mathbf{N}_i = \sum_{k=1}^{3} C_{ik}(\zeta_1, \zeta_2, \zeta_3)\mathbf{s}_k, \tag{37}$$

where

$$\mathbf{s}_1 = \nabla\zeta_2 \times \nabla\zeta_3, \tag{38}$$

$$C_{i1} = \frac{\partial N_{i3}}{\partial \zeta_2} - \frac{\partial N_{i2}}{\partial \zeta_3}, \tag{39}$$

and similarly by permutation of indices one can compute $\mathbf{s}_2$, C_{i2}, $\mathbf{s}_3$, C_{i3}.

Substituting vector shape function $\mathbf{N}_i$, and its curl $\nabla \times \mathbf{N}_i$ into (10) and (11) gives

$$K_{ij} = \int_{\hat{\Omega}} \frac{1}{\epsilon}\left(\sum_{k=1}^{3} C_{ik}(\zeta_1, \zeta_2, \zeta_3)\mathbf{s}_k\right)\cdot\left(\sum_{l=1}^{3} C_{jl}(\zeta_1, \zeta_2, \zeta_3)\mathbf{s}_l\right) J\,\mathrm{d}\hat{\Omega}, \tag{40}$$

$$M_{ij} = \int_{\hat{\Omega}} \mu\left(\sum_{k=1}^{3} N_{ik}(\zeta_1, \zeta_2, \zeta_3)\nabla\zeta_k\right)\cdot\left(\sum_{l=1}^{3} N_{jl}(\zeta_1, \zeta_2, \zeta_3)\nabla\zeta_l\right) J\,\mathrm{d}\hat{\Omega}, \tag{41}$$

where J is the determinant of Jacobian $\mathbf{J}$

$$\mathbf{J} = \left(\frac{\partial \mathbf{x}}{\partial \boldsymbol{\zeta}}\right)^{\mathrm{T}}. \tag{42}$$

Since non-dimensional curvilinear coordinates are independent of the actual geometry of the element, the following identities are zero

$$\frac{\partial N_{ik}}{\partial d_r} = 0, \tag{43}$$

$$\frac{\partial C_{ik}}{\partial d_r} = 0. \tag{44}$$

The expression for stiffness and mass matrix sensitivities are then

$$\begin{aligned}\frac{\partial K_{ij}}{\partial d_r} = &\int_{\hat{\Omega}} \frac{1}{\epsilon}\left(\sum_{k=1}^{3} C_{ik}\frac{\partial \mathbf{s}_k}{\partial d_r}\right)\cdot\left(\sum_{l=1}^{3} C_{jl}\mathbf{s}_l\right) J\,\mathrm{d}\hat{\Omega} + \int_{\hat{\Omega}} \frac{1}{\epsilon}\left(\sum_{k=1}^{3} C_{ik}\mathbf{s}_k\right)\cdot\left(\sum_{l=1}^{3} C_{jl}\frac{\partial \mathbf{s}_l}{\partial d_r}\right) J\,\mathrm{d}\hat{\Omega} \\ &+ \int_{\hat{\Omega}} \frac{1}{\epsilon}\left(\sum_{k=1}^{3} C_{ik}\mathbf{s}_k\right)\cdot\left(\sum_{l=1}^{3} C_{jl}\mathbf{s}_l\right)\frac{\partial J}{\partial d_r}\,\mathrm{d}\hat{\Omega},\end{aligned} \tag{45}$$

$$\begin{aligned}\frac{\partial M_{ij}}{\partial d_r} = &\int_{\hat{\Omega}} \mu\left(\sum_{k=1}^{3} N_{ik}\frac{\partial \nabla\zeta_k}{\partial d_r}\right)\cdot\left(\sum_{l=1}^{3} N_{jl}\nabla\zeta_l\right) J\,\mathrm{d}\hat{\Omega} + \int_{\hat{\Omega}} \mu\left(\sum_{k=1}^{3} N_{ik}\nabla\zeta_k\right)\cdot\left(\sum_{l=1}^{3} N_{jl}\frac{\partial \nabla\zeta_l}{\partial d_r}\right) J\,\mathrm{d}\hat{\Omega} \\ &+ \int_{\hat{\Omega}} \mu\left(\sum_{k=1}^{3} N_{ik}\nabla\zeta_k\right)\cdot\left(\sum_{l=1}^{3} N_{jl}\nabla\zeta_l\right)\frac{\partial J}{\partial d_r}\,\mathrm{d}\hat{\Omega}.\end{aligned} \tag{46}$$

The term $\frac{\partial \mathbf{s}_1}{\partial d_r}$ can be computed as

$$\frac{\partial \mathbf{s}_1}{\partial d_r} = \frac{\partial \nabla\zeta_2}{\partial d_r}\times\nabla\zeta_3 + \nabla\zeta_2\times\frac{\partial \nabla\zeta_3}{\partial d_r}. \tag{47}$$

The transformation between physical coordinate $\mathbf{x}$ and normalized coordinate $\boldsymbol{\zeta}$ for a discrete domain can be written in terms of nodal coordinates of the physical mesh

$$\mathbf{x} = \sum_{i=1}^{n_m} \phi_i(\boldsymbol{\zeta})\mathbf{x}_i, \tag{48}$$

where $\mathbf{x}_i$ is the coordinate at node i, ϕ_i is the scalar shape function, and n_m are number of mesh points.

Using (42) and (48), the derivative of the $\mathbf{J}$ with respect to the design variable d_r is given by

$$\frac{\partial \mathbf{J}}{\partial d_r} = \sum_{i=1}^{n_m} \frac{\partial \mathbf{x}_i}{\partial d_r}\left(\nabla^{\zeta}\phi_i\right)^{\mathrm{T}}, \tag{49}$$

where ∇^{ζ} is the gradient vector in the curvilinear coordinate system. The derivative of the determinant of J is then

$$\frac{\partial J}{\partial d_r} = J\sum_{i=1}^{n_m} \frac{\partial \mathbf{x}_i}{\partial d_r}\cdot\left(\nabla^{\zeta}\phi_i\right). \tag{50}$$

Similarly, by differentiating the identity $\mathbf{J}^{-1}\mathbf{J} = \mathbf{I}$, where $\mathbf{I}$ is the identity matrix, we get:

$$\frac{\partial \mathbf{J}^{-1}}{\partial d_r} = -\mathbf{J}^{-1}\frac{\partial \mathbf{J}}{\partial d_r}\mathbf{J}^{-1}. \tag{51}$$

The term $\frac{\partial \mathbf{x}_i}{\partial d_r}$ is called the *design velocity*. It reflects how the location of each grid node changes as the design variable changes. Differentiability of the objective function requires mesh differentiability, i.e. the change in nodal coordinate with respect to design variable must be continuous. For the shape determination problem,

each nodes physical position can be written as functions of shape parameters, i.e. $\mathbf{x}_i(d_r)$ in (49) and (50) is known explicitly.

We described a framework for computing the shape sensitivities for the discrete formulation. An alternative to compute the shape sensitivities of the Jacobian terms is to use finite difference method. For instance, the term $\frac{\partial}{\partial d_r}\left(\frac{\partial x_i}{\partial \zeta_j}\right)$ can also be computed using the forward difference scheme:

$$\frac{\partial}{\partial d_r}\left(\frac{\partial x_i}{\partial \zeta_j}\right) = \frac{1}{a}\left(\frac{\partial x_i}{\partial \zeta_j}(d_r + a) - \frac{\partial x_i}{\partial \zeta_j}(d_r)\right), \tag{52}$$

where a is a small perturbation in the shape parameter d_r. The result obtained by finite difference method is "exact" since the dependence of the Jacobian terms to the shape parameters is linear.

References

[1] V. Akcelik, G. Biros, J. Ghattas, O. Hill, D. Keyes, B. van Bloemen Waanders, Parallel algorithms for PDE-constrained optimization, in: M. Heroux, P. Raghaven, H. Simon (Eds.), Parallel Processing in Scientific Computing, SIAM, 2006.

[2] V. Akcelik, G. Biros, O. Ghattas, D. Keyes, K. Ko, L. Lee, E.G. Ng, Adjoint methods for electromagnetic shape optimization of the low-loss cavity for the International Linear Collider, Journal of Physics: Conference Series 16 (2005) 435–445.

[3] P.R. Amestoy, I.S. Duff, J. Koster, J.-Y. L'Excellent, A fully asynchronous multifrontal solver using distributed dynamic scheduling, SIAM Journal of Matrix Analysis and Applications 23 (1) (2001) 15–41.

[4] P.R. Amestoy, I.S. Duff, J.-Y. L'Excellent, Multifrontal parallel distributed symmetric and unsymmetric solvers, Computation Methods in Applied Mechanical Engineering 184 (2000) 501–520.

[5] J. Burkardt, M. Gunzburger, J. Peterson, Insensitive functionals, inconsistent gradients, spurious minima, and regularized functionals in flow optimization problems, International Journal of Computational Fluid Dynamics 16 (3) (2006) 171–185.

[6] M.T. Chu, G.H. Golub, Inverse Eigenvalue Problems: Theory Algorithms, and Applications, Oxford University Press, 2005.

[7] CUBIT geometry and mesh generation toolkit, <http://cubit.sandia.gov>.

[8] DESY webpage <http://tesla.desy.de>.

[9] S. Friedland, J. Nocedal, M.L. Overton, The formulation and analysis of numerical-methods for inverse eigenvalue problems, SIAM Journal on Numerical Analysis 24 (3) (1987) 634–667.

[10] T. Hallerod, D. Ericsson, A. Bondeson, Shape and material optimization using gradient methods and the adjoint problem in time and frequency domain, Compel – The International Journal of Computation and Mathematics in Electrical and Electronic Engineering 24 (3) (2005) 882–892.

[11] P.C. Hansen, Rank Deficient and Discrete Ill-Posed Problems, SIAM, 1998.

[12] J. Haslinger, P. Neittaanmäki, Finite Element Approximation for Optimal Shape, Material, and Topology Design, John Wiley & Sons, New York, 1996.

[13] K.M. Gawrylczyk, M. Kugle, Time domain sensitivity analysis of electromagnetic quantities utilizing FEM for the identification of material conductivity distributions, Compel – The International Journal of Computation and Mathematics in Electrical and Electronic Engineering 25 (3) (2006) 589–598.

[14] M. Gunzburger, Perspectives in Flow Control and Optimization, SIAM, 2003.

[15] J. Jin, Finite Element Method in Electromagnetics, second ed., John Wiley & Sons, New York, 2002.

[16] L. Lee, L. Ge, M. Kowalski, Z. Li, C. Ng, G. Schussman, M. Wolf, K. Ko, Solving large sparse linear systems in end-to-end accelerator structure simulations, in: Proc. of the 18th International Parallel and Distributed Processing Symposium. Santa Fe, New Mexico, 2004.

[17] Y.Q. Liu, P. Sousa, E. Salinas, P. Cruz, J. Daalder, Continuum gradient-based shape optimization of conducting shields for power frequency magnetic field mitigation, IEEE Transactions on Magnetics 42 (4) (2006) 1215–1218.

[18] P. Monk, Finite Element Methods for Maxwell's Equations, Oxford, 2003.

[19] J. Nocedal, S.J. Wright, Practical Optimization, Springer Series in Operational Research, 1999.

[20] J.S. Ryu, Y.Y. Yao, C.S. Koh, S. Yun, D.S. Kim, Optimal shape design of 3-D nonlinear electromagnetic devices using parameterized design sensitivity analysis, IEEE Transactions on Magnetics 41 (5) (2005) 1792–1795.

[21] D.F. Sun, J. Sun, Strong semi-smoothness of eigenvalues of symmetric matrices and its application to inverse eigenvalue problems, Siam Journal on Numerical Analysis 40 (6) (2003) 2352–2367.

[22] D.K. Sun, J.F. Lee, Z. Cendes, Construction of nearly orthogonal Nedelec bases for rapid convergence with multilevel preconditioned solvers, Siam Journal on Scientific Computing 23 (4) (2001) 1053–1076.

[23] Y. Sun, N. Folwell, Z. Li, G. Golub, High precision accelerator cavity design using the parallel eigensolver Omega3P, in: Proc. of the 18th Annual Review of Progress in Applied Computational Electromagnetics, 2002.

[24] A. Tarantola, Inverse Problem Theory and Methods for Model Parameter Estimation, SIAM, 2004.

[25] The International Linear Collider webpage <http://www.linearcollider.org>.

[26] J.P. Webb, Hierarchical vector basis functions of arbitrary order for triangular and tetrahedral finite elements, IEEE Transactions on Antennas and Propagation 47 (8) (1999) 1244–1253.

[27] L. Xiao, C. Adolphsen, V. Akcelik, A. Kabel, K. Ko, L. Lee, Z. Li, C. Ng, Modeling imperfection effects on dipole modes in Tesla cavity, in: Proc. of 2007 Particle Accelerator Conference, Albuquerque, New Mexico.